Non-linear flow in fractured rock

Olaf Kolditz
Institut für Stromungsmechanik, University of Hannover, Hannover, Germany

Received July 2000
Revised May 2001
Accepted May 2001

Keywords *Finite elements, Non-linear dynamics, Pumps*

Abstract *This paper deals with theory and computation of fluid flow in fractured rock. Non-Darcian flow behavior was observed in pumping tests at the geothermal research site at Soultz-sous-Forêts (France). Examples are examined to demonstrate the influence of fracture roughness and pressure-gradient dependent permeability on pressure build-up. A number of test examples based on classical models are investigated, which may be suited as benchmarks for non-linear flow. This is a prelude of application of the non-linear flow model to real pumping test data. Frequently, conceptual models based on simplified geometric approaches are used. Here, a realistic fracture network model based on borehole data is applied for the numerical simulations. The obtained data fit of the pumping test shows the capability of fracture network models to explain observed hydraulic behavior of fractured rock systems.*

Nomenclature

α_1, α_2	= Forchheimer coefficients
A	= cross-section area
A^e	= 1-D element area
$2b$	= mean fracture aperture
C	= cubic law coefficient
C_{ij}, $\mathbf{C}^e$	= capacitance matrix, element capacitance matrix
d	= mean asperity height
det	= determinant
D	= diffusivity coefficient
D_h	= hydraulic radius
e	= element, superscript
g, $\mathbf{g}$	= gravity acceleration
g_i	= Gaussian quadrature weighting coefficients
h	= Piezometric head
H	= fracture height
i, j	= nodal indices
$\mathbf{J}$	= Jacobian matrix
$[J_{1D}]$, $[J_{2D}]$	= Jacobian of 1-D, 2-D elements, respectively
$\mathbf{J}^{-1}$	= inverse Jacobian matrix
$[J_{1D}^{-1}]$, $[J_{2D}^{-1}]$	= inverse Jacobian of 1-D, 2-D elements, respectively
k	= permeability value for the 1-D case
$k_{\alpha\beta}$, $\mathbf{k}$	= permeability tensor
$k_0, k_{\alpha\beta}^0, \mathbf{k}_0$	= reference permeability, tensor forms
k_{rel}	= pressure gradient dependent relative permeability
$k_{\mathrm{rel}}^{x'x'}$, $k_{\mathrm{rel}}^{y'y'}$	= pressure gradient dependent relative permeability in x', y' direction
$[k]$	= iteration number
$K_{\alpha\beta}$, $\mathbf{K}$	= hydraulic conductivity tensor
$K_0, \mathbf{K}_0$	= reference hydraulic conductivity, tensor form
K_{rel}	= head gradient dependent relative permeability
K_{ij}, $\mathbf{K}^e$	= conductivity matrix, element conductivity matrix

This work was supported in part by the Institute of Geoscientific Research (GGA) in Hannover. In particular the encouragement of Daniel Pribnow and Christoph Clauser is gratefully acknowledged. The author would like to thank Abderrahmane Habbar, René Kaiser, Thomas Rother, Carsten Thorenz from the Groundwater Modeling Group of the Institute of Fluid Mechanics for cooperation in realising the new object-oriented concept of Rockflow-3. The helpful hints of Michaela Hunze, Martin Kohlmeier and Sylvia Moenickes concerning the manuscript are gratefully acknowledged. Special thanks are extended to the reviewers for their very instructive hints.

International Journal of Numerical Methods for Heat & Fluid Flow, Vol. 11 No. 6, 2001, pp. 547-575.

L = fracture length
L^e = 1-D element length
n = porosity
ngp = number of Gaussian points (quadrature)
ne = number of elements
np = number of nodes
$[n]$ = time step number (superscript)
Ne = von Neumann number
N_i, $\mathbf{N}$ = shape functions
p = fluid pressure
q, $\mathbf{q}$ = Darcy velocity, seepage velocity
Q = fluid volumetric source, volumetric injection rate
Q_ρ^h = fluid mass source term with respect to piezometric head
Q_ρ^p = fluid mass source term with respect to fluid pressure
r_i, $\mathbf{r}^e$ = right-hand-side term, element vector
r, s, t = local element coordinates
Re = Reynolds number
Re_{crit} = critical Reynolds number
Re^l_{crit} = critical Reynolds number for laminar non-linear flow
Re^t_{crit} = critical Reynolds number for turbulent flow
REV = representative elementary volume
S = domain boundary
S_0^h = specific storativity with respect to piezometric head
S_0^p = specific storativity with respect to fluid pressure
$t, \Delta t$ = time, time step increment
$\mathbf{T}$ = coordinate transformation matrix
x_α, x_β = physical Cartesian coordinates
x', y' = physical element coordinates
$\mathbf{x}$ = physical Cartesian coordinate vector
z = elevation
α, β = coordinate indices (1, 2, 3)
γ = non-linear flow parameter
λ = hydraulic drag or friction coefficient
μ = dynamic viscosity
ν = kinematic viscosity
ρ = fluid density
$\epsilon = d/2b$ = fracture roughness
$\omega_i, \boldsymbol{\omega}$ = weighting functions, vector
$\phi_i, \boldsymbol{\phi}$ = interpolation functions, vector
θ_t = time collocation point $0 \leq \theta_t \leq 1$
Ω, Ω^e = model domain, element
$\partial\Omega$ = boundary of model domain
∇ = nabla operator $\nabla_r = [\partial/\partial r]^T$, $\nabla_{rs} = [\partial/\partial r, \partial/\partial s]^T$
Δ = difference operator
$[_{1D}]$, $[_{2D}]$ = 1-D, 2-D finite element matrix
$[\ldots]$, $[\ldots]^T$ = Nodal matrix and transposed form
$\{\ldots\}$ = Nodal vector
$\hat{u}$ = hat denotes approximation of function u

1. Introduction

Fractured rocks are strongly heterogeneous media. Fractured rock consists of different structural components such as matrix blocks and fractures with varying orientations as well as different length scales. Owing to their geometric complexity several conceptual models were developed in the past, such as continua approaches (e.g. Barenblatt *et al.*, 1990) and discrete fracture approaches (e.g. Witherspoon *et al.*, 1980; Brown, 1987) as well as combinations of both. In this paper we consider crystalline rocks, where water flows mainly through fractures. Therefore, we are dealing with discrete fracture models.

At low flow velocities, the average flow on a macroscopic scale through a fracture is normally described using a two-dimensional version of the same equations as those used to model flow in porous media (Darcy's law). Darcy (1856) found experimentally that the volume of fluid percolating through a sand column is proportional to the applied pressure difference:

$$Q = qA = A\frac{k}{\mu}\frac{\Delta p}{L} \quad \rightarrow \quad \Delta p = \frac{L}{A}\frac{\mu}{k}Q, \tag{1}$$

where Q is the volumetric flow rate, which is Darcy velocity q multiplied by tube cross-section area A, L is the column length and k/μ is a hydraulic resistance.

Various authors (e.g. Bear, 1972; Scheidegger, 1974; Diersch, 1985) have considered the derivation of Darcy's law from the underlying Navier-Stokes equations for flow in the pores of a porous medium by a spatial averaging procedure over a representative elementary volume (REV) containing many pores. Such studies have provided considerable support for Darcy's law.

$$\mathbf{q} = -\frac{\mathbf{k}}{\mu}(\nabla p - \rho \mathbf{g}), \tag{2}$$

where $\mathbf{q}$ is the Darcy or seepage velocity vector, $\mathbf{k}$ is the permeability tensor of the porous medium, μ is fluid dynamic viscosity and $\mathbf{g}$ is the gravity acceleration.

Darcy's law is based essentially on the assumption that fluid motion is inertialess, i.e. inertial terms can be neglected with regard to viscous forces. Thus, Darcian flow is a special case of creeping flow for which viscous forces prevail over inertial forces.

In groundwater hydraulics, frequently, piezometric head $h = p/g\rho + z$ (for homogeneous fluids) is used instead of fluid pressure p. Then the Darcy equation is:

$$\mathbf{q} = -\mathbf{K}\nabla h, \tag{3}$$

where $\mathbf{K} = (\rho g/\mu)\,\mathbf{k}$ is the hydraulic conductivity tensor of the porous medium.

In a general porous medium, Darcy's law breaks down with increasing flow velocity, well before the onset of true turbulence (Barenblatt *et al.*, 1990; Dybbs and Edwards, 1984). The linear relationship between pressure drop and flow rate Q becomes invalid if convective acceleration and/or transient effects become important. The first case is denoted by *non-linear laminar flow*, when inertial effects become important, e.g. due to curvature of pores or channeling in fractures. The second case is related to *turbulent flow*, when flow pattern becomes transient due to velocity fluctuations. Therefore, we have to distinguish between three different flow regimes: linear laminar flow, non-linear laminar flow and "true" turbulent flow. Confusion between non-linear laminar flow and "true" turbulent flow may arise from the fact that inertia effects in laminar flow are expressed in the same fashion as in turbulent flows concerning the relationship between pressure drop and the flow rate:

$$\Delta p = a_1 Q + a_2 Q^2. \tag{4}$$

This relationship is known as the Forchheimer equation. It was introduced by Forchheimer (1914) for pipe and channel flows, originally. Comparing equations (1) and (4), the additional drag term in non-linear flows becomes obvious. Deviations from linearity between seepage velocity and pressure drop

are denoted as non-Darcian flow. Physical causes underlying non-linear effects can be high flow rates, molecular effects, ionic effects and non-Newtonian behavior of the fluid itself (Scheidegger, 1974; Dullien, 1979). Morphological causes for non-linear effects can be pore geometry (pores are curved, have varying cross-sections, may be sealed, and suffer from dead-end effects).

For fracture hydraulics, Witherspoon *et al.* (1980) have shown that, for a parallel-sided fracture, the flow can be described by Darcy's law, if transmissivity of the fracture is given by the cubic law (equation (8)). However, if fractures are rough or the flow velocities are high, Darcy's law is not applicable. In analogy to the effects of pore geometry in porous media, fracture roughness as well as fracture intersections in networks may be reasons for non-linear flow phenomena in fractured media. Lomize (1951) developed empirical laws to model flow in fractures with significant roughness. Louis (1967), Romm (1966) and Lomize (1951) showed that flow in fractures is turbulent for Reynolds numbers larger than about 2,300, necessitating a modification of the flow equations (see section 2).

In this paper, a numerical study of non-linear flow in fractures is presented. Possible models for the flow are presented, numerical modeling using finite elements is discussed, some simple examples are analysed and then modeling for a real site is undertaken. In particular, we will focus on modeling effects of high flow rates (see subsection 5.2) and fracture roughness (see subsection 5.3) causing additional drags due to increasing inertial forces.

2. Experimental issues

Important numbers in engineering hydraulics in order to evaluate flow regimes are the Reynolds number Re and the hydraulic resistance coefficient λ. The Reynolds number, which relates inertial to viscous forces, is defined as:

$$Re = \frac{\rho q D_h}{\mu}, \tag{5}$$

where D_h is the hydraulic radius, which is a characteristic length scale of the flow process. Friction or hydraulic resistance coefficient is defined as (Zielke, 1990):

$$\lambda = \frac{2D_h}{\rho q^2}\frac{\Delta p}{L}. \tag{6}$$

The critical parameter for determination of Reynolds numbers and friction coefficients is the characteristic length scale for flow processes – the hydraulic radius D_h.

Using Darcy's law (equation (1)) we can easily derive relationships between Reynolds number, friction factor, seepage velocity and permeability:

$$\lambda = \frac{1}{Re}\frac{2D_h^2}{k},\ Re = \frac{1}{\lambda}\frac{2D_h^2}{k},\ q = \frac{2\mu D_h}{\rho k}\frac{1}{\lambda} = \frac{Re}{D_h}\frac{\mu}{\rho},\ k = \frac{1}{\lambda}\frac{2D_h^2}{Re}. \tag{7}$$

The characteristic length scale D_h for porous media is based on a mean value of grain diameters. The order of critical Reynolds numbers, when non-linear effects become evident, determined in experiments is about 1-10 (Barenblatt *et al.*, 1990). The corresponding velocities are only in the range of millimeters or centimeters per second. For comparison, the critical Reynolds number dividing laminar from turbulent flow regimes in tubes with a circular cross-section is about $Re_{\text{crit}} = 2{,}300$. It is obvious that critical Reynolds numbers for porous media are much less than critical Reynolds numbers of flow through straight tubes with a circular cross-section. Therefore, it is questionable that turbulence, i.e. additional drag terms due to Reynolds stresses, resulting from velocity fluctuations in time, is responsible for non-linear flow phenomena. Transient phenomena related to "true" turbulence in porous media were observed by Dybbs and Edwards (1984) at Reynolds numbers larger than 100.

In general, linear and non-linear flow regimes in porous media do not change immediately. There is a transition zone between the two regimes because of the range of pore radii and the corresponding velocity variations. Couland *et al.* (1986) found those transition effects by numerical modeling of flow through cylinder arrays. They found that linear flow is valid up to $Re^{l}_{\text{crit}} < 1$ and a quadratic flow law is valid beginning with $Re^{t}_{\text{crit}} < 13$. In the intermediate case, there can coexist areas with both linear and non-linear flow regimes.

Witherspoon *et al.* (1980) conducted experiments in rock fractures to study hydraulic behavior. They proved the "cubic law" for the transmissivity of a fracture consisting of parallel planar plates:

$$Q = C(2b)^3 \Delta p, \tag{8}$$

where $2b$ is the fracture aperture, and C is a constant depending on flow geometry and fluid properties. This relationship means that fracture flow can be described by Darcy's law, using an equivalent hydraulic permeability. When choosing the hydraulic radius for fractures equal to double fracture aperture $D_h = 4b$, we yield a friction factor $\lambda = 96/Re$, which is equal to that value for parabolic flow profiles in plane channels. Fracture permeability is then $k = (2b)^2/12$ (see Table I).

Friction factor λ	Permeability k	Reference
Darcy (1856) $\frac{96}{Re}$	$\frac{(2b)^2}{12}$	[7]
Louis (1967) $\frac{96}{Re}\left[1 + 8.8\epsilon^{3/2}\right]$	$\frac{(2b)^2}{12}\frac{1}{1 + 8.8\epsilon^{3/2}}$	[22]
Lomize (1951) $\frac{96}{Re}\left[1 + 6\epsilon^{3/2}\right]$	$\frac{(2b)^2}{12}\frac{1}{1 + 17\epsilon^{3/2}}$	[21]

Table I.
Linear flow friction factors and permeabilities

Beside hydraulic conditions, such as high flow rates, geometric properties such as fracture roughness can influence the flow behavior. One of the first comprehensive works on flow through fractures was given by Lomize (1951). He investigated the effect of fracture roughness using parallel glass plates with rough surfaces for his experiments. Lomize (1951) introduced the concept of defining fracture roughness, $\epsilon = d/2b$, in terms of mean asperities height, d. He developed several empirical equations for friction factors as a function of both Reynolds number and fracture roughness, $\lambda(Re, \epsilon)$. If the fracture roughness is larger than $\epsilon > 0.032$, permeability becomes significantly depending of it – $k(D_h, \epsilon)$ (see Table II). Commonly by this critical value of roughness, fracture flow is divided into parallel and non-parallel motion (i.e. velocity components normal to the fracture plane arise from asperities). Moreover, fracture roughness can cause channeling effects in fracture planes (Brown, 1987; Moreno *et al.*, 1988; Tsang, 1992).

Figure 1 shows simulated fracture aperture and resulting velocity distribution within a rough fracture (Kolditz, 1997). Fracture aperture distribution was generated using a fractal model. The channelized velocity field gives an idea about the importance of local accelerations in fracture flow.

In the case in which the quadratic term in the Forchheimer equation (4) dominates, this equation can be rewritten as:

$$\Delta p = a_2 Q^2 \quad \Rightarrow \quad Q = \underbrace{\frac{\sqrt{L}}{\sqrt{a_2 \Delta p / L}}}_{k/\mu} \frac{\Delta p}{L}, \tag{9}$$

we see, that permeability becomes dependent on pressure gradients (Table II):

Friction factor λ	Permeability k	Reference
Blasius (1913) $\lambda = \dfrac{0.316}{Re^{1/4}}$	$\dfrac{\mu}{\rho}\left[\dfrac{(2b)^5 \rho^4}{\mu}\right]^{1/7}\left[\dfrac{\partial p}{\partial x}\right]^{-3/7}$	[2]
Nikuradse (1930) $\dfrac{1}{\sqrt{\lambda}} = \left\lvert 2\log\left(\dfrac{\epsilon}{3.7}\right)\right\rvert$	$\dfrac{4g\mu\sqrt{2b}}{\sqrt{\rho}}\log\dfrac{3.7}{\epsilon}\left[\dfrac{\partial p}{\partial x}\right]^{-1/2}$	[24]
Louis (1967) $\dfrac{1}{\sqrt{\lambda}} = \left\lvert 2\log\left(\dfrac{\epsilon}{1.9}\right)\right\rvert$	$\dfrac{4g\mu\sqrt{2b}}{\sqrt{\rho}}\log\dfrac{1.9}{\epsilon}\left[\dfrac{\partial p}{\partial x}\right]^{-1/2}$	[22]
Lomize (1951) $\dfrac{1}{\sqrt{\lambda}} = \left\lvert 2.55\log\left(\dfrac{\epsilon}{1.24}\right)\right\rvert$	$\dfrac{5.11g\mu\sqrt{2b}}{\sqrt{\rho}}\log\dfrac{1.24}{\epsilon}\left[\dfrac{\partial p}{\partial x}\right]^{-1/2}$	[21]

Table II.
Non-linear flow friction factors and permeabilities

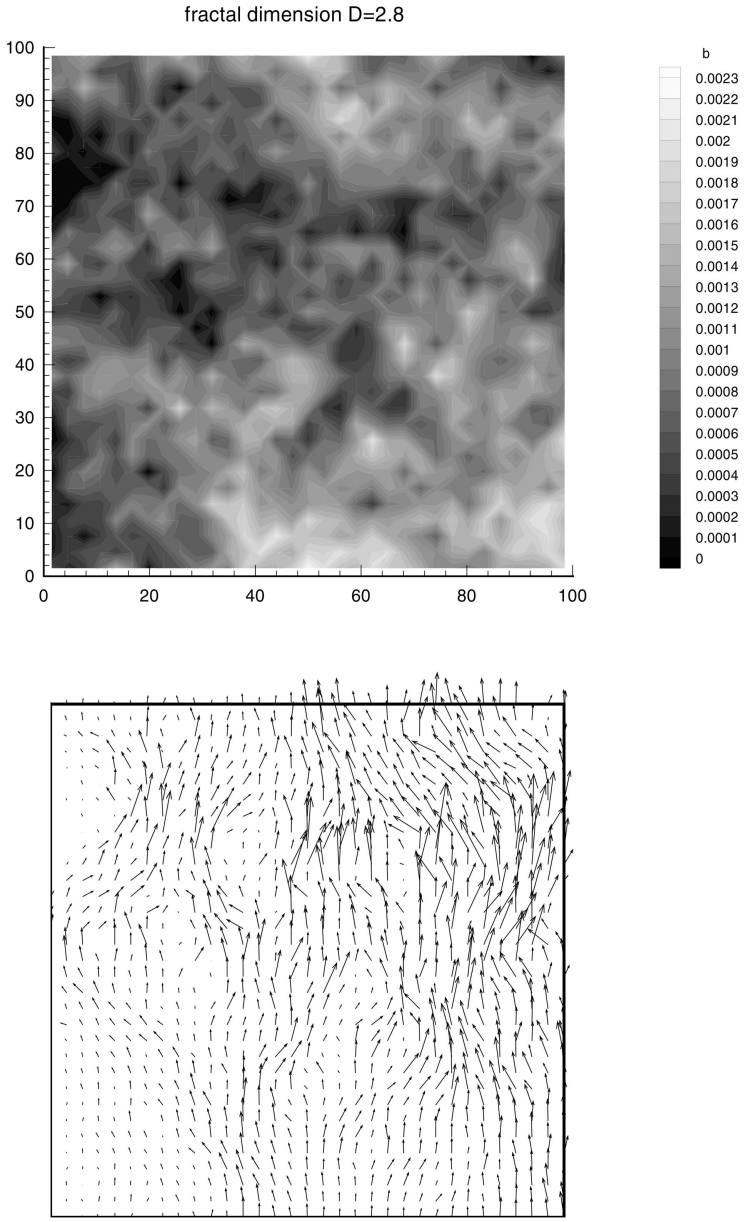

Figure 1.
Fracture aperture pattern (top) and velocity distribution (bottom) within a rough fracture

$$k = \frac{\mu}{\rho}\frac{\sqrt{\rho D_h}}{\sqrt{\lambda}}\left(\frac{\Delta p}{L}\right)^{-1/2} = \underbrace{\frac{\nu\sqrt{D_h}}{\lambda g}}_{k_0}\left(\frac{\Delta p/\rho g}{L}\right)^{-1/2}. \tag{10}$$

In contrast to porous media flow, critical Reynolds numbers at the transition

from laminar to turbulent flow were found to be in the order of 2,300 for fractures (Louis, 1967). Romm (1966) and Lomize (1951) reported the critical value to be as much as 2,400. This means that critical Reynolds numbers for fracture flow are in the same order as those for tube flows. These values are about two orders of magnitude larger than those for porous medium flow.

Louis (1967) considered the similarity between tube, channel and fracture flows. He adapted existing relationships for tube and channel flows to fractures. Based on experiments, he modified friction factors to fracture flow for linear (Table I) and non-linear regimes (Table II). Blasius (1913) originally determined the friction factor for smooth tubes in the range $2{,}320 < Re < 10^5$. Nikuradse (1930) considered slightly rough tubes with non-circular cross-sections. However, it is questionbly, whether these critical Reynolds numbers are valid for natural fractures providing significant roughness.

As a summary of classic hydraulic approaches, Figure 2 illustrates the above discussed models for linear and non-linear flow in smooth as well as rough fractures.

3. Governing equations

In this section we give a brief summary of the equations governing flow in a porous medium. A two-dimensional version of these equations also describes flow in a fracture on a macroscopic scale. Readers who are interested in more details of the derivation of the governing equations should refer to Bear (1972),

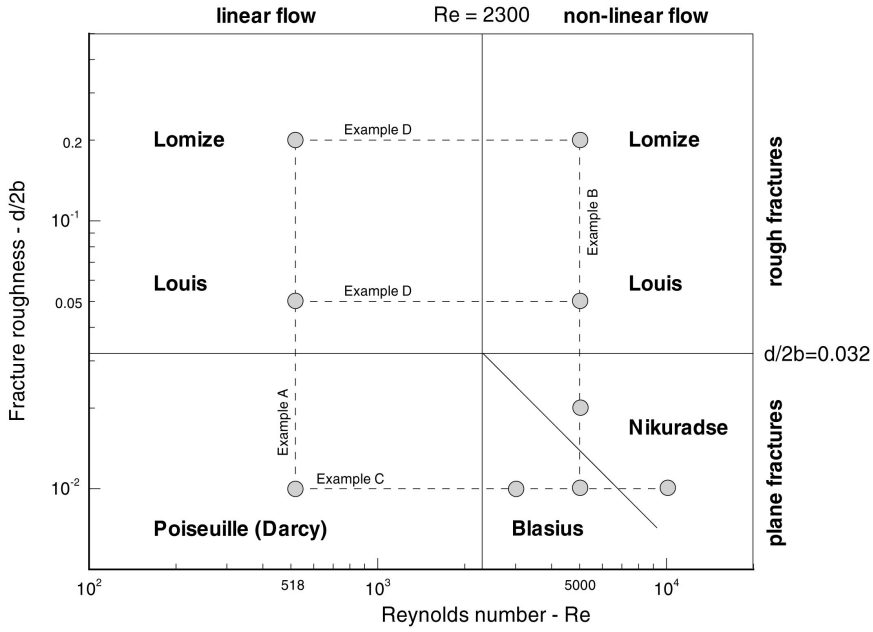

Source: Adapted from Louis (1967)

Figure 2.
Linear and non-linear flow in plane and rough fractures

Scheidegger (1974), Pinder and Gray (1977), Diersch (1985), Barenblatt *et al.* (1990) or Lewis and Schrefler (1998).

We consider isothermal flow of homogeneous liquids in a porous medium (e.g. saturated groundwater flow). We start from the differential form of the balance equation of the fluid mass. The unknown field function is fluid pressure:

$$S_0^p \frac{\partial p}{\partial t} - \nabla \cdot \mathbf{q} = Q_\rho^p. \tag{11}$$

In groundwater hydraulics, frequently, piezometric head $h = p/g\rho + z$ (for homogeneous fluids) is used instead of fluid pressure p:

$$S_0^h \frac{\partial h}{\partial t} - \nabla \cdot \mathbf{q} = Q_\rho^h, \tag{12}$$

where Q_ρ^h is the fluid mass source term with respect to piezometric head, Q_ρ^p is the fluid mass source term with respect to fluid pressure, S_0^p is the specific storativity with respect to fluid pressure, and S_0^h is the specific storativity with respect to piezometric head.

Based on the Forchheimer equation (4), we use the following generalization of Darcy's law for non-linear groundwater flow:

$$\mathbf{q} = -\mathbf{K}(h, \nabla h)\nabla h, \tag{13}$$

where the hydraulic conductivity tensor $\mathbf{K}$ is assumed to be pressure dependent. In general pressure as well as pressure gradient dependencies are assumed for compressible and/or multiphase flows. For groundwater flow (incompressible fluids) it is assumed that the influence of pressure gradients dominates (e.g. Häfner, 1985; Busch *et al.*, 1993). Then hydraulic conductivity is given by:

$$\mathbf{K}(\nabla h) = \mathbf{K}_0 \mid \nabla h \mid^{\gamma - 1} = \mathbf{K}_0 K_{\text{rel}} \tag{14}$$

$$\gamma = \begin{cases} > 1 & \text{pre-linear} \\ = 1 & \text{linear (Darcy law)} \\ < 1 & \text{post-linear} \\ & = 1/2 \text{ turbulent friction} \end{cases}. \tag{15}$$

The non-linear flow parameter γ divides three flow regimes:

(1) pre-linear;

(2) linear; and

(3) post-linear.

In the pre-linear modus, motion is restricted by electro-molecular forces attracting the fluid molecules to the solid surface. The pre-linear regime is

characterized by small pressure gradients $|\nabla h| \ll 1$, whereas the post-linear regime is characterized by large gradients $|\nabla h| \gg 1$. In the post-linear mode, motion is restricted by non-linear friction effects. From the above equation it can be seen that, the effective hydraulic resistance K_{rel} increases for smaller pressure gradients in pre-linear situations and for larger pressure gradients in post-linear situations as well.

Returning to fluid pressure p as primary variable, we use permeability instead of hydraulic conductivity. In analogy to multiphase flow theory for porous media, we introduce a relative permeability k_{rel} to separate the non-linear term of the permeability tensor:

$$\begin{aligned} \mathbf{k} &= \mathbf{k}_0 k_{\mathrm{rel}} \\ k_{\mathrm{rel}} &= |\ \nabla(p/g\rho + z)\ |^{\gamma-1}\ . \end{aligned} \tag{16}$$

The equation of fluid motion (equation (13)) can be rewritten now as:

$$\mathbf{q} = -\frac{\mathbf{k}_0}{\mu} k_{\mathrm{rel}} \nabla(p + g\rho z). \tag{17}$$

Additionally, we assume homogeneity of the fluid (i.e. constant density and viscosity). Combining both the mass and momentum balance equations we obtain the flow equation:

$$S_0^p \frac{\partial p}{\partial t} - \nabla \cdot \left(\frac{\mathbf{k}_0}{\mu} k_{\mathrm{rel}} \nabla(p + g\rho z) \right) = Q_\rho^p. \tag{18}$$

As can be seen, a non-linear flow equation results if the non-linear flow parameter γ differs from unity. In the following we use index notation to make tensor operations more obvious. For the index notation we use the Einstein summation convention for repeating indices:

$$S_0^p \frac{\partial p}{\partial t} - \frac{\partial}{\partial x_\alpha} \left(\frac{k^0_{\alpha\beta}}{\mu} k_{\mathrm{rel}} \frac{\partial}{\partial x_\beta} (p + g\rho z) \right) = Q_\rho^p. \tag{19}$$

Flow in a fracture is described by a two-dimensional version of this equation. For treating networks each fracture is considered as a plane in 3D Euclidean space. Fractures are connected by their intersection traces. The required coordinate transformations are given in the Appendix (2D non-linear flow elements in $\mathcal{R}^3$). For transformation of spatial derivatives we need Jacobian matrices.

4. Numerical scheme

4.1 Galerkin method

The use of the method of weighted residuals provides an integral formulation of the flow equation to obtain the approximate solution:

$$\int_\Omega \omega_i \left[S_0^p \frac{\partial \hat{p}}{\partial t} - \frac{\partial}{\partial x_\alpha} \left(\frac{k^0_{\alpha\beta}}{\mu} k_{\mathrm{rel}} \left(\frac{\partial \hat{p}}{\partial x_\beta} + \rho g \frac{\partial \hat{z}}{\partial x_\beta} \right) \right) \right] d\Omega = \int_\Omega \omega_i Q^p_\rho d\Omega, \tag{20}$$

where $\boldsymbol{\omega} = \{\omega_i\}$ (weighting functions) and Ω is the model domain.

The unknown function p is approximated by a trial solution $\hat{p}$:

$$p(t, x_\alpha) \approx \hat{p}(t, x_\alpha) \equiv \sum_{j=1}^{np} \phi_j(x_\alpha) p_j(t), \tag{21}$$

$$z(x_\alpha) \approx \hat{z}(x_\alpha) \equiv \sum_{j=1}^{np} \phi_j(x_\alpha) z_j, \tag{22}$$

where $\phi = \{\phi_i\}$ (interpolation functions), p_j is the nodal value of pressure, z_j is the nodal value of elevation, and m is the number of nodes.

According to the Bubnov-Galerkin method we use identical weighting $\boldsymbol{\omega}$ and interpolation function $\boldsymbol{\phi}$:

$$\int_\Omega \phi_i \left[S_0^p \phi_j \frac{dp_j}{dt} - \frac{\partial}{\partial x_\alpha} \left(\frac{k^0_{\alpha\beta}}{\mu} k_{\mathrm{rel}} \left(\frac{\partial \phi_j}{\partial x_\beta} p_j + \rho g \frac{\partial \phi_j}{\partial x_\beta} z_j \right) \right) \right] d\Omega = \int_\Omega \phi_i Q^p_\rho d\Omega. \tag{23}$$

Partial integration is used to reduce the order of the derivatives:

$$\begin{aligned} &\int_\Omega \phi_i \left[S_0^p \phi_j \frac{dp_j}{dt} + \frac{\partial \phi_j}{\partial x_\alpha} \left(\frac{k^0_{\alpha\beta}}{\mu} k_{\mathrm{rel}} \left(\frac{\partial \phi_j}{\partial x_\beta} p_j + \rho g \frac{\partial \phi_j}{\partial x_\beta} z_j \right) \right) \right] d\Omega \\ &= - \int_{\partial\Omega} \phi_i q_n dS + \int_\Omega \phi_i Q^0_\rho d\Omega, \end{aligned} \tag{24}$$

with the outward flux vector:

$$q_n = - \frac{k^0_{\alpha\beta}}{\mu} k_{\mathrm{rel}} \left(\frac{\partial \hat{p}}{\partial x_\beta} + \rho g \frac{\hat{\partial} z}{\partial x_\beta} \right) n_\alpha. \tag{25}$$

We rearrange the above equation to put the unknown terms to the left-hand side only:

$$\begin{aligned} &\int_\Omega \phi_i \left[S_0^p \phi_j \frac{dp_j}{dt} + \frac{\partial \phi_j}{\partial x_\alpha} \frac{k^0_{\alpha\beta}}{\mu} k_{\mathrm{rel}} \frac{\partial \phi_j}{\partial x_\beta} p_j \right] d\Omega \\ &= - \int_\Omega \phi_i \frac{\partial \phi_j}{\partial x_\alpha} \frac{k^0_{\alpha\beta}}{\mu} k_{\mathrm{rel}} \rho g \frac{\partial \phi_j}{\partial x_\beta} z_j d\Omega \\ &\quad - \int_{\partial\Omega} \phi_i q_n dS + \int_\Omega \phi_i Q^p_\rho d\Omega. \end{aligned} \tag{26}$$

This equation forms a global system of equations where the number of equations corresponds to the number of grid points:

$$C_{ij}\frac{dp_j}{dt} + K_{ij}(\hat{p})p_j = r_i, \quad i,j = 1,\ldots,np, \tag{27}$$

with:

$$\begin{aligned} C_{ij} &= \int_\Omega \phi_i S_0^p \phi_j \, d\Omega, \\ K_{ij}(\hat{p}) &= \int_\Omega \frac{\partial \phi_i}{\partial x_\alpha} \frac{k^0_{\alpha\beta}}{\mu} k_{\mathrm{rel}} \frac{\partial \phi_j}{\partial x_\beta} \, d\Omega, \\ r_i(\hat{p}) &= -\rho g K_{ij}(\hat{p}) z_j - \int_{\partial\Omega} \phi_i q_n dS + \int_\Omega \phi_i Q^p_\rho d\Omega. \end{aligned} \tag{28}$$

The resolution of non-linearities as well as time discretization are described in section 4.4.

4.2 Finite element approach

Decomposition of the computation domain into finite elements:

$$\Omega = \bigcup_{e=1}^{ne} \Omega^e, \quad \partial\Omega = \bigcup_{e=1}^{ne} \partial\Omega^e, \tag{29}$$

means that the global matrices can be composed by its element contributions:

$$C_{ij} = \sum_{e=1}^{ne} C^e_{ij}, \quad K_{ij} = \sum_{e=1}^{ne} K^e_{ij}, \quad r_i = \sum_{e=1}^{ne} r^e_i. \tag{30}$$

Interpolation functions ϕ correspond now to individual elements and shape functions $\mathbf{N}$ are used for interpolation at the element level:

$$\begin{aligned} \hat{p}^e &= N_j(\mathbf{x})\, p_j(t), \\ N_j &= \begin{cases} 1, & \mathbf{x} = \mathbf{x}_j \\ 0, & \text{at remaining grid nodes} \end{cases} \end{aligned} \tag{31}$$

where $\mathbf{x}$ is the coordinate vector and $\mathbf{x}_j$ is the coordinate vector of node j.

Element matrices (equation (29)) are written in terms of shape functions:

$$
\begin{aligned}
C_{ij}^{e} &= \int_{\Omega^e} N_i S_0^p N_j \, d\Omega, \\
K_{ij}^{e}(\hat{p}) &= \int_{\Omega^e} \frac{\partial N_i}{\partial x_\alpha} \frac{k_{\alpha\beta}}{\mu} k_{\mathrm{rel}} \frac{\partial N_j}{\partial x_\beta} \, d\Omega^e, \\
r_i^e(\hat{p}) &= -\rho g K_{ij}^{e}(\hat{p}) z_i - \int_{\partial\Omega^e} N_i q_n dS + \int_{\Omega^e} N_i Q_\rho^p d\Omega.
\end{aligned}
\tag{32}
$$

4.3 Evaluation of element matrices in local coordinates

Transformation from physical (x, y, z) to local (r, s, t) coordinates, e.g. by isoparametric functions, allows the evaluation of element matrices in unit coordinates. We return at this point to vector notation to keep the equations compact:

$$
\begin{aligned}
C_{ij}^{e} &= \int_{\Omega^e} N_i S_0^p N_j \, d\Omega, \\
\mathbf{C}^{e} &= \int_{\Omega^e} \mathbf{N} S_0^p \mathbf{N} \, d\Omega \\
&= \int_{-1}^{+1} \int_{-1}^{+1} \int_{-1}^{+1} \mathbf{N} S_0^p \mathbf{N} \underbrace{\det \mathbf{J} \, drdsdt}_{d\Omega^e},
\end{aligned}
\tag{33}
$$

$$
\begin{aligned}
K_{ij}^{e} &= \int_{\Omega^e} \frac{\partial N_i}{\partial x_\alpha} \frac{k_{\alpha\beta}}{\mu} k_{\mathrm{rel}} \frac{\partial N_j}{\partial x_\beta} \, d\Omega^e, \\
\mathbf{K}^{e} &= \int_{\Omega^e} \nabla \mathbf{N} \frac{1}{\mu} \mathbf{k}_0 k_{\mathrm{rel}} \nabla \mathbf{N}^T \, d\Omega^e \\
&= \int_{-1}^{+1} \int_{-1}^{+1} \int_{-1}^{+1} \underbrace{\nabla \mathbf{N} (\mathbf{J}^{-1})^T}_{\nabla \mathbf{N}(x,y,z)} \frac{1}{\mu} \underbrace{\mathbf{T}^T \mathbf{k}_0 k_{\mathrm{rel}} \mathbf{T}}_{\mathbf{k}(x,y,z)} \\
&\quad \underbrace{\nabla \mathbf{N}^T \mathbf{J}^{-1}}_{\nabla \mathbf{N}^T(x,y,z)} \underbrace{\det \mathbf{J} \, drdsdt}_{d\Omega^e},
\end{aligned}
\tag{35}
$$

$$
\begin{aligned}
r_i^e &= -\rho g K_{ij}^{e}(\hat{p}) z_i - \int_{\partial\Omega^e} N_i q_n dS + \int_{\Omega^e} N_i Q_\rho^p d\Omega, \\
\mathbf{r}^e &= -\rho g \mathbf{K}^{\mathbf{e}}(\hat{p}) \mathbf{z} - \int_{\partial\Omega^e} \mathbf{N} q_n dS + \int_{-1}^{+1} \int_{-1}^{+1} \int_{-1}^{+1} \mathbf{N} Q_\rho^p \det \mathbf{J} \, drdsdt,
\end{aligned}
\tag{35}
$$

where $\mathbf{J}$ is the Jacobian matrix and $\mathbf{T}$ is the ordinary coordinate transformation matrix. This general finite element approach, described above, allows coupling

of multi-dimensional elements (1D/2D/3D) positioned arbitrarily in 3D space. The specification of above finite element formulations for linear 1D and bilinear 2D element types is given in the Appendix.

4.4 Resolution of the non-linearities

For large flow rates, the effects of non-Darcian flow have to be taken into account. In this case, hydraulic permeability is no longer a constant but it depends on the pressure gradient. Non-linear flow behavior results in a non-linear flow equation, which is resolved by use of the Picard (fixpoint) iteration procedure.

The flow equation (19) is rewritten to emphasize the solution process:

$$S_0^p \frac{\partial p^{[k]}}{\partial t} - \frac{\partial}{\partial x_\alpha}\left(\frac{k^0_{\alpha\beta} k^{[k-1]}_{\mathrm{rel}}}{\mu}\left(\frac{\partial p^{[k]}}{\partial x_\beta} + \rho g \frac{\partial z}{\partial x_\beta}\right)\right) = Q^p_\rho, \tag{36}$$

where $[k]$ is the new iteration level and $[k-1]$ is the prior one. The pressure gradient dependent permeability is evaluated at the old iteration level. Velocities can be calculated at each time level by:

$$q_\alpha = -\frac{k^0_{\alpha\beta} k^{[k]}_{\mathrm{rel}}}{\mu}\left(\frac{\partial p^{[k]}}{\partial x_\beta} + \rho g \frac{\partial z}{\partial x_\beta}\right), \tag{37}$$

where $[k]$ is the final iteration step.

For time discretization we return to matrix equation (29). All terms are evaluated at the intermediate time point $t + \theta_t \Delta t$:

$$C_{ij} \frac{dp_j}{dt} \mid_{t+\theta_t \Delta t} + K_{ij}(\hat{p}) p_j \mid_{t+\theta_t \Delta t} = r_i \mid_{t+\theta_t \Delta t} . \tag{38}$$

Linear interpolation in time yields:

$$\begin{aligned} &C_{ij}\left[\frac{p_j(t+\Delta t) - p_j(t)}{\Delta t}\right] + K_{ij}(\hat{p})\left[(1-\theta_t)p_j(t) + \theta_t p_j(t+\Delta t)\right] \\ &= \left[(1-\theta_t) r_i(t) + \theta_t r_i(t+\Delta t)\right], \end{aligned} \tag{39}$$

where the unknown function and the right-hand-side terms are weighted in time. This way, explicit and implicit schemes can be selected easily.

Rearranging the above terms, new time level to the left and old time level to the right-hand side, we obtain:

$$\begin{aligned} &\left[\frac{1}{\Delta t} C_{ij} + \theta_t K^{[k-1][n]}_{ij}\right] p_j^{[k][n]} = \left[\frac{1}{\Delta t} C_{ij} - (1-\theta_t) K^{[n-1]}_{ij}\right] p_j^{[n-1]} \\ &+ (1-\theta_t) r_i(t)^{[n-1]} + \theta_t r_i^{[k-1][n]}, \end{aligned} \tag{40}$$

where [n], [$n-1$] are new and old time levels, respectively, and [k], [$k-1$] are new and old iteration levels, respectively.

The numerical scheme is implemented in the object-oriented simulation system Rockflow (Kolditz *et al.*, 1999). In the next two sections we apply the non-linear flow model to single fracture and fracture network simulations.

5. Non-linear flow in single fractures

In this section we consider flow through single fractures with rectangular shape (Figure 3). In general, several one-, two- and three-dimensional finite elements are at the disposal of the finite element simulator Rockflow (Kolditz *et al.*, 1999). We use one-dimensional elements for borehole and two-dimensional elements for fracture representations. If fracture-matrix interaction has to be taken into account, e.g. for simulation of heat extraction from hot, dry rocks (Kolditz and Clauser, 1998), additionally three-dimensional elements for rock matrix representation have to be added.

In particular, we are interested in the effects of non-linear flow behavior due to large seepage velocities (section 5.2) and the effects of fracture roughness (section 5.3). Common simulation parameters for all case studies are given in Table III. Fracture permeabilities are selected corresponding to the models by Darcy (1856), Blasius (1913), Nikuradse (1930), Lomize (1951) and Louis (1967) (see Tables I and II). For large Reynolds numbers fracture permeability depends on both fracture roughness and pressure gradient. Table IV presents a summary of specific model parameters.

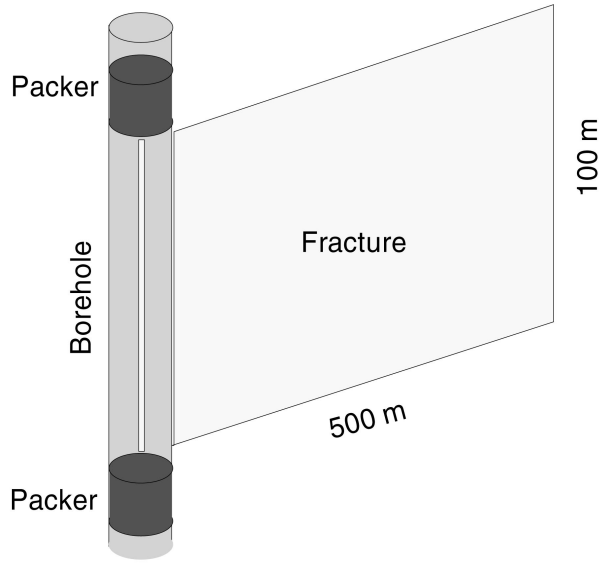

Figure 3.
Single fracture model

5.1 Numerical properties

The first study concerns *stability* and *accuracy* of the numerical scheme. For numerical stability we have to satisfy the von Neumann criterion for diffusion type equations:

$$Ne = \frac{\Delta t D}{\Delta x^2} \leq \frac{1}{2}. \tag{41}$$

This stability criterion relates both temporal and spatial discretizations. Diffusivity coefficient for pressure equation (19) is defined as:

$$D = \frac{\|\mathbf{k}\| k_{\text{rel}}}{\mu S_0^p}. \tag{42}$$

Table III.
Common simulation parameters (water at $T = 130°C$, $p = 35MPa$)

Symbol	Quantity	Value
L	Fracture length	500m
H	Fracture height	100m
$2b$	Hydraulic fracture aperture	41×10^{-4}m
$S_0^p = S_0^h/g\rho$	Specific storativity of the fracture	$10^{-3} - 10^{-7}$ Pa^{-1}
Q	Injection rates	$(6 - 116) \times 10^{-3}$ m3 s^{-1}
μ	Dynamic viscosity of water	2.2×10^{-4} Pa s
ρ	Density of water	950kgm^{-3}

Table IV.
Overview of single fracture case studies

	Linear flow		Non-linear flow	
Very rough	**Case A3** Re = 518 $d/2b$ = 0.2 K = 0.23543ms^{-1} Lomize		**Case B4** Re = 5,000 $d/2b$ = 0.2 K = 0.24803ms^{-1} Lomize	
Rough	**Case A2** Re = 518 $d/2b$ = 0.05 K = 0.54026ms^{-1} Louis		**Case B3** Re = 5,000 $d/2b$ = 0.05 K = 0.45191ms^{-1} Louis	
Plane	**Case A1/C1** Re = 518 $d/2b$ < 0.032 K = 0.59341ms^{-1} Darcy	**Case C2** Re = 1,123 $d/2b$ < 0.032 K = 0.59341ms^{-1} Darcy	**Case B2** Re = 5,000 $d/2b$ = 0.02 K = 0.59341ms^{-1} Nikuradse	
$d/2b$ < 0.032			**Case B1** Re = 5,000 $d/2b$ < 0.05 K = 0.59341ms^{-1} Blasius	**Case C4** Re = 10,000 $d/2b$ = 0.01 K = 0.59341ms^{-1} Blasius
	Re > 2,300		Re > 2,300	

From criterion (equation (41)) we derive the following restriction to time step length:

$$\Delta t \leq \frac{1}{2}\frac{\Delta x^2 \mu S_0^p}{\|\mathbf{k}\| k_{\text{rel}}}. \tag{43}$$

Violating the von Neumann criterion yields oscillating numerical solutions.

At first we consider the steady state behavior. For this purpose we assume a linear flow regime. In this case the steady state pressure level directly corresponds to the Reynolds number. Figure 4 depicts pressure build-up for different fracture velocities (Table V). For this study, we selected flow rates corresponding to pumping test conditions at the Soultz site and to empirical models of interest (Figure 2). Doubling the Reynolds number (e.g. $Re = 5{,}000 \rightarrow 10{,}000$) has to result in doubled pressure difference (e.g. $p = 1.1 \times 10^7 \rightarrow 2.2 \times 10^7$) at the steady state level.

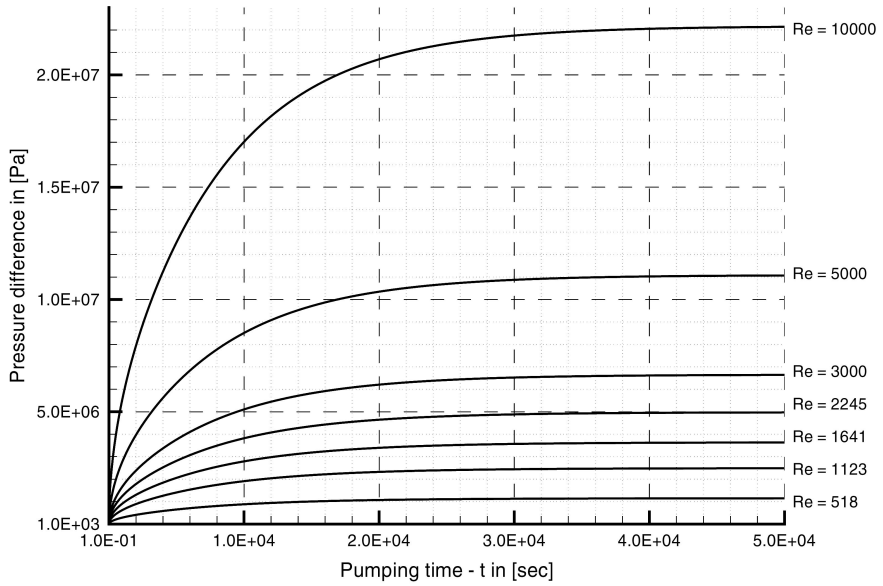

Figure 4.
Pressure build-up during linear flow in smooth fractures

q in $[m^3 s^{-1}]$	Re
6×10^{-3}	518
1.3×110^{-2}	1,123
1.9×10^{-2}	1,641
2.6×10^{-2}	2,245
3.47368×10^{-2}	3,000
5.78947×10^{-2}	5,000
1.15789×10^{-1}	10,000

Table V.
Flow rates and corresponding Reynolds numbers

After testing stability based on the von Neumann criterion, now we investigate the accuracy of numerical solutions. To this purpose we conduct a grid convergence study. The calculations were undertaken using several consecutively refined meshes, beginning with a spatial resolution from $\Delta x = 50$m to $\Delta x = 0.625$m. To avoid effects of grid anisotropy, the vertical discretization was identical to the horizontal one, i.e. $\Delta x = \Delta z$. The corresponding time discretizations due to the von Neumann criterion (equation (43)) is given in Table VI. Results of the grid convergence test are presented in Figures 5 and 6. Figure 5 shows the effect of grid refinement on pressure build-up over the entire pumping time. Differences of the numerical solutions occur, in particular, in the early time period up to ten seconds. Beginning with resolutions smaller than $\Delta x = 1.25$ we obtain nearly identical results for pressure increase. Pressure profiles along the fracture for a selected time point ($t = 10^4$, s) are given in Figure 6. The results converge for resolutions smaller than $\Delta x = 5$m. As a result of this accuracy test we use grids with the resolution of

Table VI.
Spatial and temporal discretization for grid convergence test

Δx in [m]	Δt in [s]
50	100
20	16
10	4
5	1
2.5	0.25
1.25	0.0625
0.625	0.015625

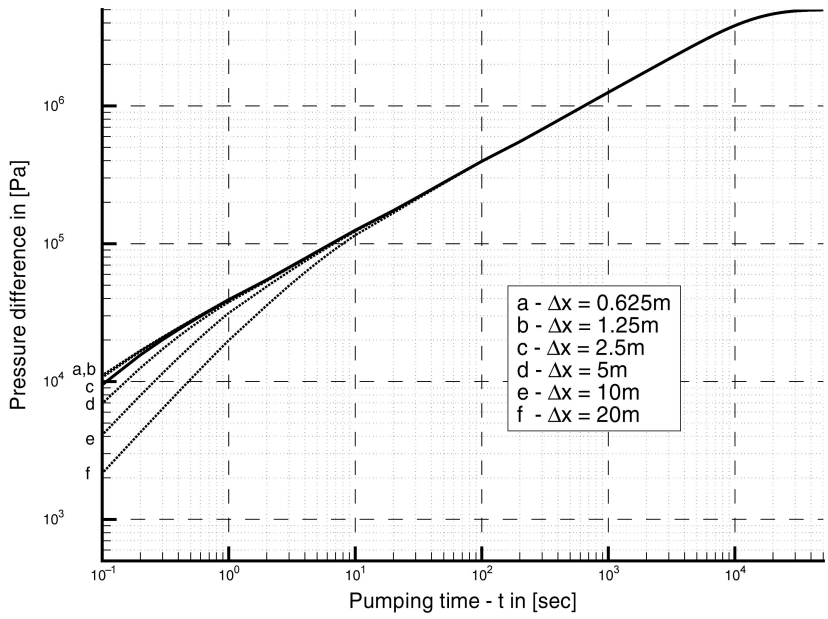

Figure 5.
Grid convergence test – temporal pressure increase in the injection borehole

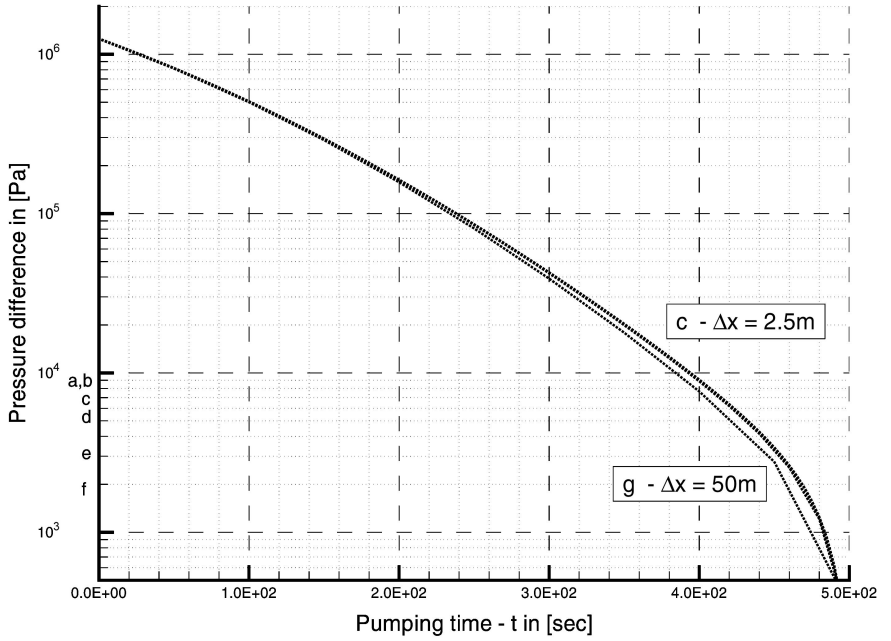

Figure 6.
Grid convergence test – pressure increase along fracture at $t = 10^4 s$

$\Delta x = \Delta z = 2.5$m for the single fracture models. Time steps were selected with respect to the von Neumann criterion (Table VI).

The accuracy test due to temporal and spatial discretization has been done for linear flow. For the accuracy of the non-linear flow simulations we have to select an appropriate error tolerance for the iteration procedure (see section 4.4). To keep the numerical error due to the linearization process smaller than due to the selected discretization, we use an error tolerance of $\| p^{k+1} - p^k \| \leq 10^3 \, Pa$.

5.2 Effects of non-linearity

After getting more confidence in the numerical scheme we turn to effects of non-linear flow behavior. However, we have to keep in mind that the von Neumann criterion is strictly valid only for linear problems.

To investigate linear and non-linear flow regimes in plane fractures (e.g. $d/2b = 0.01$), different flow rates are forced through the fracture (Table V). These examples correspond to models by Darcy (1856), Blasius (1913), and Nikuradse (1930) (Figure 2). Figure 7 presents the resulting pressure build-up curves for linear and non-linear flow behavior. We obtain the following results:

- Non-linear effects become important for Reynolds numbers larger than $Re > 2{,}245$. For Re = 2,245 we observe a slight deviation from linear flow behavior in the steady state phase. This is in good agreement with the range of critical Reynolds numbers $Re_{\text{crit}} \in$ [2,300-2,400] found by Lomize (1951), Romm (1966) and Louis (1967) for smooth fractures. With increasing Reynolds numbers the deviation from linear flow behavior

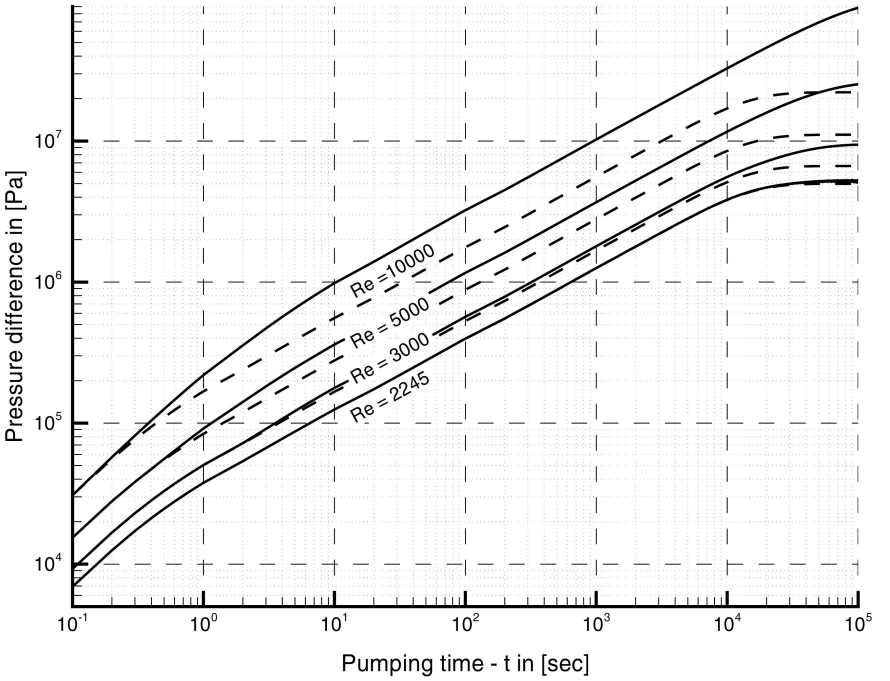

Figure 7.
Effects of non-linear flow in smooth fractures (Cases C from Table IV)

becomes more and more significant. For Re = 10,000 the pressure required to force the 116 liters per second through the fracture is more than four times larger due to non-linear flow effects.

- Whereas, the pressure increase during the transient stage is very similar (i.e. shapes of curves), non-linear effects have a strong influence on the onset of steady state flow. The more non-linear the flow is, the later steady state is reached, i.e for larger Reynolds numbers steady state flow will be reached later.

5.3 Fracture roughness

Now we study the influence of fracture roughness for linear and non-linear flows.

Figure 8 shows the computed pressure build-up curves for different values of fracture roughness under linear flow conditions (i.e. models by Darcy (1856), Louis (1967) and Lomize (1951)). In the parenthesises of the figure captions the simulation cases (capital letters) are given according to Table IV and Figure 2.

The next simulations concern pressure transients during non-linear flow. This example was selected to capture the empirical models by Blasius (1913), Nikuradse (1930), Louis (1967) and Lomize (1951), displayed in Figure 2. Reynolds number was chosen to be Re = 5,000. Certainly, this is a large number for pumping test situations in natural fractures, resulting in large pressure values. Figure 9 shows the computed pressure increase at the fracture entry for

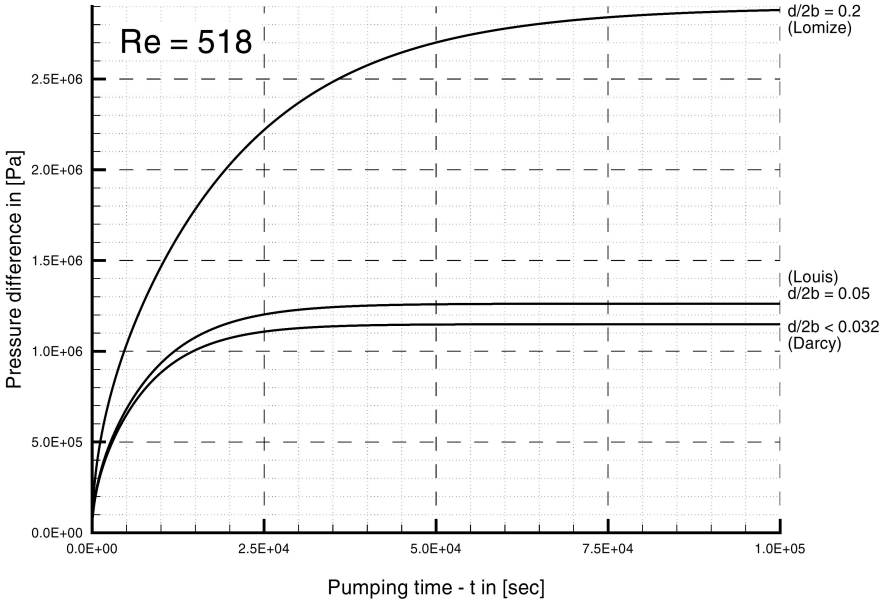

Figure 8.
Pressure build-up during linear flow for different values of fracture roughness (Cases A1, A2 and A3 from Table IV)

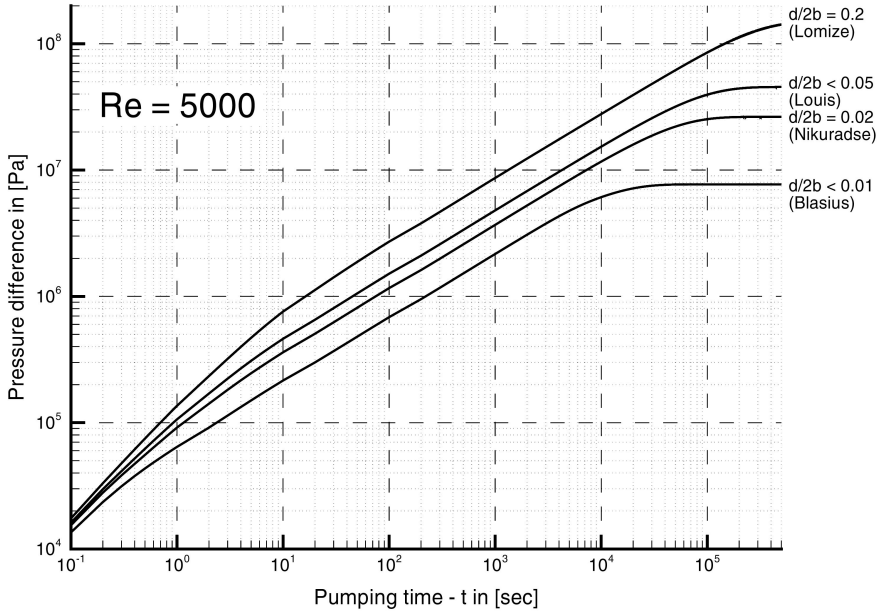

Figure 9.
Pressure build-up during non-linear flow for different values of fracture roughness (Cases B1, B2, B3 and B4 from Table IV)

different values of fracture roughness. We draw the following conclusions from both examples:

- reduced hydraulic conductivity due to larger fracture roughness requires larger pressure differences to inject a certain fluid volume into the fracture;

- steady state flow is reached after a considerably longer time than in plane or less rough fractures.

6. Non-linear flow in fracture systems

This section deals with non-linear flow behavior in natural fracture systems. Data for this study are from the geothermal research program at Soultz-sous-Forõts in France. Data were provided by the Geoscientific Research Institute (GGA) (Pribnow and Clauser, 1999). Non-linear flow behavior was observed from high-rate pumping tests at the Soultz site (Jung *et al.*, 1995). The subject of this research program is the utilization of geothermal energy from hot, dry rock systems. The experimental area is located in deep crystalline rocks about 3,500m in depth. Recently, a new reservoir at 5,000m depth was created. The Soultz fracture network model consists of seven fractures representing the observed main flow paths in the crystalline location. The geometry of the fracture network as reconstructed from borehole logging as well as the generated finite element grid are shown in Figure 10. Geometric modeling of fracture networks and mesh generation of intersecting planes is described in detail by Rother *et al.* (2000). Numerical simulations of non-linear flow and, in particular, of transport processes require sufficiently good mesh qualities. The finite element discretization used for this study consists of 4,829 nodes and 5,296 quadrilateral elements. Element sizes vary from about 50m to 1m. Element meshes are finer, in particular, in the fracture intersection areas. The time stepping scheme was adapted in the following way. Time steps of ten seconds were used for the transient stages and time steps of 100 seconds were used for quasi steady-state periods of each flow rate increase step.

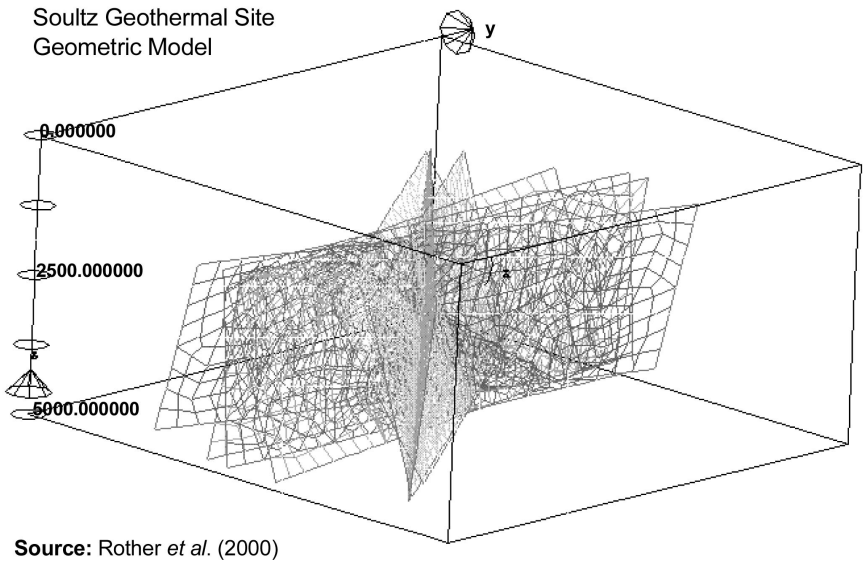

Source: Rother *et al.* (2000)

Figure 10.
Fracture network model and finite element discretization

Kohl *et al.* (1997) analysed two prior pumping tests (94JUN16, 94JUL04) conducted in the Soultz geothermal reservoir by using a finite element model. Their geometric model was a conceptual approach consisting of one fracture embedded in the rock matrix. Real geometry of the hydraulically active fracture system was neglected in their studies. The purpose of our study is to investigate non-linear flow behavior using data-based fracture network models (Figure 10).

Figure 11 shows simulations of pumping test 95JUL01 conducted at the Soultz site (Jung *et al.*, 1995). Circles illustrate measured data and solid lines mark simulated pressure for both cases of linear flow (Darcy) and non-linear flow (Forchheimer). Linear flow behavior shows a linear relationship between pumping rate increase and corresponding pressure increase to force the fluid volume through the system (lower solid curve in Figure 11). The pumping test clearly indicates non-linear flow behavior. The flow rates of the four steps increase nearly in a linear stepwise way: $6\,ls^{-1}$, $13\,ls^{-1}$, $19\,ls^{-1}$ and $26\,ls^{-1}$. As can be seen from Figure 11, the pressure increase is nearly quadratical. Parameters required for the data fit are given in Table VII The range of parameters found by Kohl *et al.* (1997) for the two prior pumping tests is also plotted in Table VII. It can be seen that permeability values are close but storativity values differ. Note, storativity values by Kohl *et al.* (1997) correspond to the rock matrix, whereas our values correspond to the fracture system. In fact, this is the conceptual difference between both models. Kohl *et al.* (1997) assumed that fluid can be stored in the rock matrix. We think that in the short time scale of the experiment fluid loss into the rock matrix must be very small and, therefore, we assume that the fluid is stored in the fracture system. If relating both storativity values by the rock porosity of about $n = 10^{-3}$, we see that the volume of storable fluid is comparable for both models.

From Figure 11 it can be seen that the pumping test data are well matched by using the non-linear flow model except the shut-off period. During this period fluid pressure is decreasing to the hydrostatic level. The overestimated pressure drawdown means that the storativity of the reservoir is underestimated in the shut-off period. This indicates storativity changes during the hydraulic tests. This can be explained with the increased volume of the stimulated fracture system. Because of small relative displacements of rough fracture surfaces during pressure increase they will not close perfectly after reducing the reservoir pressure again. Those effects of residual apertures after loading and unloading of rough fractures was observed, e.g. by Brown (1987). We repeated the simulations with increased storativity coefficient in the shut-off period by factor 2 and 3. The corresponding curves in Figure 12 show a better fit now in the shut-off period. However, we should be careful with changing parameters not to change the underlying physical model. If storativity values change dramatically, we have to consider mechanical effects of fracture deformation.

All simulations run with time step length according to the von Neumann criterion (equation (41)). About five to ten iterations were needed to achieve

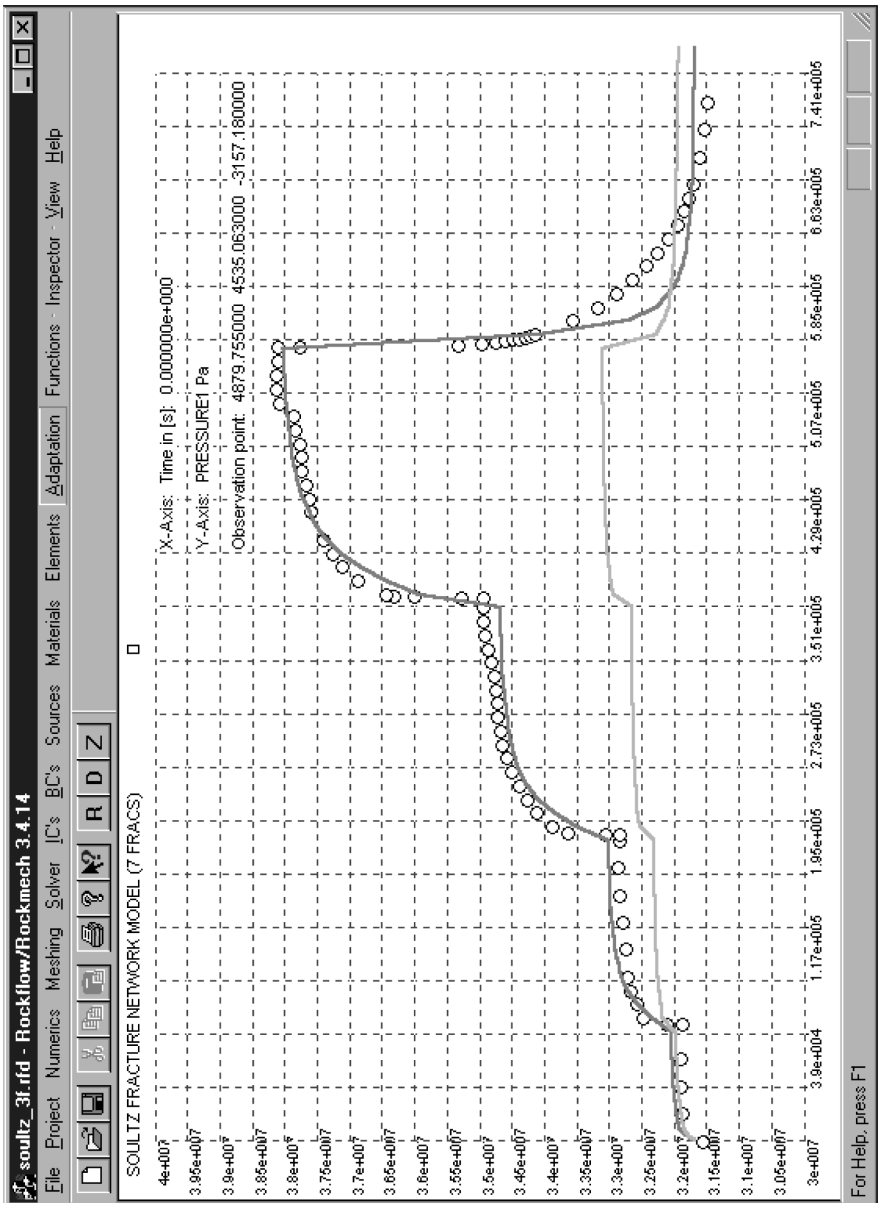

Figure 11.
Analysis of pumping test data – Darcy versus Forchheimer models

Reference permeability (k_0)	Specific storativity (S_0^p)	Non-linear flow parameter (γ)
Present study		
$3.1 \times 10^{-9} m^2$	5×10^{-6} (fracture)	0.48
Kohl et al. *(1997)*		
$[0.53 - 12] \times 10^{-9} m^2$	$10^{-9} - 2 \times 10^{-11}$ (rock matrix)	0.5 [15]

Table VII.
Simulation parameter

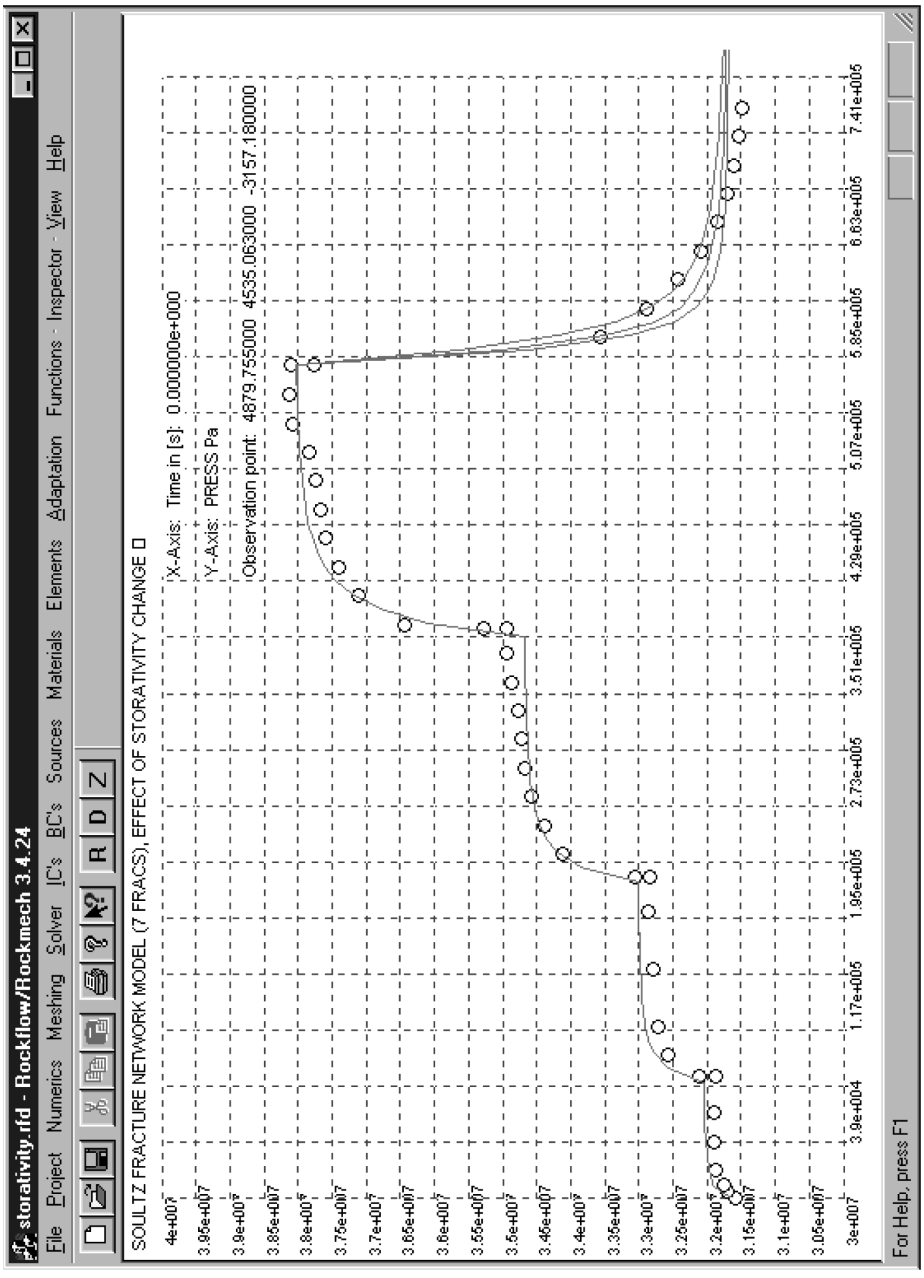

Figure 12.
Analysis of pumping test data – effect of storativity change

satisfactory convergence during updating the pressure gradient dependent permeabilities according to equation (16).

These are the first results of the pumping test evaluation and attempt to show that fracture network models in combination with non-linear flow models are capable analysing pumping tests in fractured rock. Fracture network models are able to represent both real system geometry and hydromechanical processes. In the specific case of pumping test 95JUL01, the packer interval covered two fracture intersections. Therefore, the hydraulic regime is clearly affected by radial flow effects. Accurate approximation of the real flow field is even more important for analysis of tracer transport through natural rock systems. For transport simulations with sharp concentration fronts the use of grid adaptation methods becomes necessary (Kaiser *et al.*, 1999).

7. Concluding remarks

In this paper we have investigated non-linear flow behavior in fractured systems. Single fracture examples are examined to study the influence of non-linear flows effects and fracture roughness. Empirical models by Darcy (1856), Blasius (1913), Nikuradse (1930), Lomize (1951) and Louis (1967) are used to calculate the corresponding values of fracture permeability. For smooth fractures we found good agreement between critical Reynolds numbers for onset of non-linear flow behavior known from experiments and from numerical simulations. Non-linear flow phenomena and fracture roughness lead to reduction of effective permeabilities. Additionally, the onset of steady state flow is significantly delayed. These benchmark simulations for single fractures were a prelude to analysis of pumping test data from the Soultz site. A realistic fracture network model was set up which is based on geologic data. The pumping test data could be well reproduced by applying the non-linear flow model. Questions remain with respect to the evaluation of critical Reynolds numbers for natural (rough) fractures, in particular, for more complex flow conditions. Another topic of further investigations is storativity of fracture systems. To this purpose mechanical properties (deformation) should be considered in detail.

References and further reading

Bear, J. (1972), *Dynamics of Fluids in Porous Media*, American Elsevier, New York, NY.

Blasius, H. (1913), *Das ähnlichkeitsgesetz bei Reibungsvorgôngen in Flüssigkeiten*, Forsch. Ing.-Wesen, VDI-Heft 131.

Barenblatt, G.I., Entov, V.M. and Ryzhik, V.M. (1990), *Theory of Fluid Flows through Natural Rocks*, Kluwer Academic Publishers, Dordrecht.

Brown, S.R. (1987), "Fluid flow through rock joints: the effect of surface roughness", *J. Geophysical Research*, Vol. 92 No. B2, pp. 1337-47.

Busch, K.-F., Luckner, L. and Thiemer, K. (1993), "Geohydraulik", in Matthess, G. (Hrsg.), Lehrbuch der Hydrogeologie, Band 3, Gebrüder Borntraeger Verlag, Berlin-Stuttgart.

Couland, O., Morel, P. and Caltagirone, J.-P. (1986), "Effects non linéaires dans les écoulements en milieu poreux", *C.R. Acad. Sci.*, Ser. 2 Vol. 302, pp. 263-6.

Darcy, H. (1856), *Les fontaines publiques de la ville de Dijon*, Dalmont, Paris.

Diersch, H.-J.G. (1985), *Modellierung und numerische Simulation geohydrodynamischer Transportprozesse*, Habilitationsschrift, Akademie der Wissenschaften der DDR, Berlin.

Dullien, F.A.L. (1979), *Porous Media, Fluid Transport and Pore Structure*, Academic Press, New York, NY.

Dybbs, A. and Edwards, R.V. (1984), "A new look at porous media fluid mechanics – Darcy to turbulent", in Bear and Corapcioglu (Eds), *Fundamentals of Transport Phenomena in Porous Media*, Dordrecht Publisher, Boston, MA, pp. 201-56.

Forchheimer, P. (1914), *Hydraulik*, Teubner Verlag, Berlin-Leipzig.

Häfner, F. (1985), *Geohydrodynamische Erkundung von Erdöl-, Erdgas- und Grundwasserlagerstätten*, Wissenschaftlich-Technischer Informationsdienst des Zentralen Geologischen Instituts, Vol. 26, Berlin.

Jung, R., Willis-Richards, J., Nicholls, J.D., Bertozzi, A. and Heinemann, B. (1995), "Evaluation of hydraulic test at Soultz – European HDR site", *Proc. Worlds Geothermal Congress*, Florenz, pp. 2575-80.

Kaiser, R., Kolditz, O. and Rother, T. (1999), "Modelling of flow in fractured aquifers using automatic grid adaptation", *Proc. XXVIII IAHR Conference on Hydraulic Engineering for Sustainable Water Resources Management*, Graz.

Kohl, T., Evans, K.F., Hopkirk, R.J., Jung, R. and Rybach, L. (1997), "Observation and simulation of non-Darcian flow transients in fractured rock", *Water Res. Research*, Vol. 33 No. 3, pp. 407-18.

Kolditz, O. (1997), *Strömung, Stoff- und Wôrmetransport im Kluftgestein*, Borntraeger Verlag, Berlin-Stuttgart.

Kolditz, O. and Clauser, C. (1998), "Numerical simulation of flow and heat transfer in fractured crystalline rocks: application to the hot dry rock site at Rosemanowes (UK)", *Geothermics*, Vol. 27 No. 1, pp. 1-23.

Kolditz, O., Habbar, A., Kaiser, R., Rother, T. and Thorenz, C. (1999), *ROCKFLOW – Theory and Users Manual*, Release 3.4, Groundwater Modeling Group, Institute of Fluid Mechanics, University of Hannover (www.rockflow.de).

Lamb, H. (1932), *Hydrodynamics*, Cambridge University Press, Cambridge, MA.

Lewis, R.W. and Schrefler, B.A. (1998), *The Finite Element Method in the Static and Dynamic Deformation and Consolidation of Porous Media*, Wiley & Sons, New York, NY.

Lomize, G.M. (1951), *Seepage in Fissured Rocks*, State Press, Moscow-Leningrad.

Louis, C. (1967), *Strömungsvorgänge in klüftigen Medien und ihre Wirkung auf die Standsicherheit von Bauwerken und Böschungen im Fels*, Mitteilungen des Instituts für Boden- und Felsmechanik, Heft 23, Universität Karlsruhe, Karlsruhe.

Moreno, L., Tsang, Y.W., Tsang, C.F., Hale, F.V. and Neretnieks, I. (1988), "Flow and tracer transport in a single fracture: a stochastic model and its relation to some field observations", *Water Res. Research*, Vol. 24 No. 12, pp. 2033-48.

Nikuradse, J. (1930), "Turbulente Strömungen in nicht-kreisförmigen Rohren", *Ing. Arch.*, Vol. 1, pp. 306-32.

Pinder, G.F. and Gray, W.G. (1977), *Finite Element Simulation in Surface and Subsurface Hydrology*, Academic Press, New York, NY, London.

Pribnow, D. and Clauser, C. (1999), *Heat and Fluid Flow in the Rhein Graben: Regional and Local Models for a HDR System*, Technical Report, Institut für Geowissenschaftliche Gemeinschaftsaufgaben (GGA).

Romm, E.S. (1966), *Seepage Properties of Fractured Rock* (in Russian), Nedra Publisher, Moscow.

Rother, T., Kolditz, O., Zielke, W. and Taniguchi, T. (2000), *Geometric Analysis of Fractured-Porous Aquifers*, Rockflow-Preprint [2000-3], Groundwater Modeling Group, Institute of Fluid Mechanics, University of Hannover, accepted for publication by *J Environmental Geology*.

Scheidegger A.E. (1974), *The Physics of Flow through Porous Media*, 3rd ed., University of Toronto Press, Toronto.

Tsang, Y.W. (1992), "Usages of equivalent apertures for rock fractures as derived from hydraulic and tracer tests", *Water Res. Research*, Vol. 28 No. 5, pp. 1451-5.

Witherspoon, P.A., Wang, J.S.Y., Iwai, K. and Gale, J.E. (1980), "Validity of cubic law for fluid flow in a deformable rock fracture", *Water Res. Research*, Vol. 16 No. 6, pp. 1016-24.

Zielke, W. (1990), *Strömungsmechanik für Bauingenieure*, Eigenverlag, Institut für Strömungsmechanik, Universität Hannover, Hannover.

Appendix. FE matrices

1D non-linear flow element in $\mathcal{R}^3$

Pressure-dependent permeability for non-linear flow along the 1D element is given by:

$$\begin{aligned} k'_x &= k_0 \left| \frac{\partial h}{\partial x'} \right|^{1-\gamma} = k_0 \left| \frac{\partial}{\partial x'} \left(\frac{p}{g\rho} + z \right) \right|^{1-\gamma} \\ &= k_0 \left| [J_{1D}^{-1}][\nabla_r N]^T \left(\frac{\hat{p}}{g\rho} + \hat{z} \right) \right|^{1-\gamma} \\ &= k_0 \left| \frac{(p_2 - p_1)/g\rho + (z_2 - z_1)}{L^e} \right|^{1-\gamma} \\ &= k_0 \, k_{\text{rel}}. \end{aligned} \tag{44}$$

The element conductivity matrix for non-linear flow can be developed explicitly for a 1D linear finite element:

$$\begin{aligned} [K_{1D}^e] &= \int_{\Omega^e} \begin{bmatrix} \nabla N_1 \\ \nabla N_2 \end{bmatrix} \frac{k_{x'}^e}{\mu} [\nabla N_1 \ \nabla N_2] \, d\Omega^e \\ &= A^e \int_{L^e} \begin{bmatrix} \partial N_1/\partial x' \\ \partial N_2/\partial x' \end{bmatrix} \frac{k_{x'}^e}{\mu} [\partial N_1/\partial x' \ \partial N_2/\partial x'] \, dx' \\ &= \frac{k_0^e}{\mu} \left| \frac{p_2 - p_1}{g\rho} + (z_2 - z_1) \right|^{1-\gamma} \frac{A^e}{(L^e)^{1-\gamma}} \times \\ &\quad \int_{-1}^{+1} \begin{bmatrix} \partial N_1/\partial r \\ \partial N_2/\partial r \end{bmatrix} [J_{1D}^{-1}]^T [J_{1D}^{-1}] [\partial N_1/\partial r \ \partial N_2/\partial r] \det[J_{1D}] \, dr \\ &= \frac{k_0^e}{\mu} \left| \frac{p_2 - p_1}{g\rho} + (z_2 - z_1) \right|^{1-\gamma} \frac{A^e}{(L^e)^{2-\gamma}} \begin{bmatrix} 1 & -1 \\ -1 & 1 \end{bmatrix} \\ &= k_{\text{rel}} \frac{k_0^e}{\mu} \frac{A^e}{L^e} \begin{bmatrix} 1 & -1 \\ -1 & 1 \end{bmatrix} \end{aligned} \tag{45}$$

A pressure-based formulation is preferred, therefore the gravity term has to be evaluated separately. This can be done easily using the above element conductivity matrix:

$$\begin{aligned} \{g_{1D}^e\} &= [K_{1D}^e] \times g\rho\{z\} \\ &= \int_{\Omega^e} \begin{bmatrix} \nabla N_1 \\ \nabla N_2 \end{bmatrix} \frac{k_{x'}^e(p)}{\mu} g\rho [\nabla N_1 \quad \nabla N_2] \, d\Omega^e \times \{z\} \\ &= k_{\text{rel}} \frac{k_0^e}{\mu} g\rho (z_1 - z_2) \frac{A^e}{L^e} \begin{bmatrix} 1 \\ -1 \end{bmatrix}, \end{aligned} \tag{46}$$

with the nodal vector of elevations for a 1D finite element:

$$\{z\} = \begin{Bmatrix} z_1 \\ z_2 \end{Bmatrix} \tag{47}$$

2D non-linear flow element in $\mathcal{R}^3$

Using a pressure-based formulation we have to split the piezometric head gradient in the following way:

$$\begin{bmatrix} \dfrac{\partial h}{\partial x'} \\ \dfrac{\partial h}{\partial y'} \end{bmatrix} = [\nabla_{x'y'} h] = \left[\nabla_{x'y'}\left(\frac{p}{g\rho} + z\right)\right] = \left[J_{2D}^{-1}\right][\nabla_{rs} N]^T \left(\frac{\{p\}}{g\rho} + \{z\}\right). \tag{48}$$

For convenience we formulate the pressure gradient dependent permeability for the following cases:

- General anisotropic case:

$$\begin{bmatrix} k_{x'x'} & k_{x'y'} \\ k_{y'y'} & k_{y'x'} \end{bmatrix} = [\mathbf{k}'] = \left[\mathbf{k}'_0\right]\left[\left[J_{2D}^{-1}\right][\nabla_{rs} N]^T \left(\frac{\{p\}}{g\rho} + \{z\}\right)\right]^{1-\gamma}. \tag{49}$$

- Orthotropic case ($k_{x'y'} = k_{y'x'} = 0$):

$$\begin{bmatrix} k_{x'x'} \\ k_{y'y'} \end{bmatrix} = k'_0\left[\left[J_{2D}^{-1}\right][\nabla_{rs} N]^T \left(\frac{\{p\}}{g\rho} + \{z\}\right)\right]^{1-\gamma} = k'_0 \begin{bmatrix} k_{x'x'}^{\mathrm{rel}} \\ k_{y'y'}^{\mathrm{rel}} \end{bmatrix}. \tag{50}$$

- Isotropic case:

$$k' = k'_0\left[\sqrt{\left(\frac{\partial(p/g\rho + z}{\partial x'}\right)^2 + \left(\frac{\partial(p/g\rho + z)}{\partial y'}\right)^2}\right]^{1-\gamma} = k'_0\, k_{\mathrm{rel}}. \tag{51}$$

For the orthotropic case the 2D element conductance matrix is given by:

$$\begin{aligned} [K_{2D}^e] &= \int_{\Omega^e} \begin{bmatrix} \nabla N_1 \\ \nabla N_2 \\ \nabla N_3 \\ \nabla N_4 \end{bmatrix} \frac{k'_0}{\mu} \begin{bmatrix} k_{x'x'}^{\mathrm{rel}} & 0 \\ 0 & k_{y'y'}^{\mathrm{rel}} \end{bmatrix} [\,\nabla N_1 \quad \nabla N_2 \quad \nabla N_3 \quad \nabla N_4\,]\, d\Omega^e \\ &= L^e \int_{-1}^{+1}\int_{-1}^{+1} [N]\left[J_{2D}^{-1}\right]^T \frac{k'_0}{\mu} \begin{bmatrix} k_{x'x'}^{\mathrm{rel}} & 0 \\ 0 & k_{y'y'}^{\mathrm{rel}} \end{bmatrix} \left[J_{2D}^{-1}\right][N]^T \det[J_{2D}]\, drds \\ &= L^e \sum_{i=1}^{ngp}\sum_{j=1}^{ngp} g_i g_j [N]\left[J_{2D}^{-1}\right]^T \frac{k'_0}{\mu} \begin{bmatrix} k_{x'x'}^{\mathrm{rel}} & 0 \\ 0 & k_{y'y'}^{\mathrm{rel}} \end{bmatrix} \left[J_{2D}^{-1}\right][N]^T \det[J_{2D}]. \end{aligned} \tag{52}$$

The terms have to be evaluated in the corresponding Gaussian points. The gravity term can be easily evaluated using the above element conductivity matrix:

$$\{g_{2D}^e\} = [K_{2D}^e(p)] \times g\rho\{z\}, \tag{53}$$

with the nodal vector of elevations for a 2D finite element:

$$\{z\} = \begin{Bmatrix} z_1 \\ z_2 \\ z_3 \\ z_4 \end{Bmatrix}. \tag{54}$$